4
Materials Prospects in $Cu_2HgSn(Se_xS_{1-x})_4$

4.1 Introduction

Rigorous efforts are made on quaternary chalcogens, e.g., $Cu_2ZnSn(S/Se)_4$-based alloys, to develop cost-effective materials for multiple optoelectronic and energy applications. For instance, similar to chalcopyrite, the $Cu_2ZnSn(Se_x/S_{1-x})_4$ has been studied in detail and found to possess an energy bandgap ranging from 1.5 to 1.0 eV, allowing them for multijunction solar cells as well as thermoelectric and infrared detector devices (S. Chen et al., 2011; Nagaoka et al., 2021b). Considering the high V_{oc} deficit due to the formation of antisite defects and related defect clusters, researchers have searched other cation-substituted quaternary compositions like Cu_2BaSnS_4, $Cu_2BaGaGe_4$ etc (Y. Kim et al., 2021) where the dissimilar electronic environment and large size mismatch with Zn^{2+} ions prevent antisite defect formation. Other group II elements, like Ca, Sr, Cd, and Hg, are also suggested for achieving significant size mismatch (Kaur et al., 2017). Considering these facts, another compound named $Cu_2HgSn(Se/S)_4$, which exists in the stannite phase in contrast to the most favourable kesterite phase for the Cu_2ZnZnS_4 system, is also investigated in parallel.

Further, its selenium counterpart, $Cu_2HgSnSe_4$ with 0.8 eV bandgap, provides hope in realizing it as an active layer for demanding infrared photodetectors. Therefore, the bandgap engineering with a modification to its anion composition, namely $Cu_2HgSn(Se_xS_{1-x})_4$, can likewise be advantageous for various optoelectronics applications. In addition, given the requirement for flexible solar cell technology (J. Li et al., 2023), it is necessary to build devices such as solar cells with thin films having high elastic strength (H. K. Park et al., 2022). As a result, assessing the material's ductility and mechanical strength is crucial for exploring flexible surfaces. The alloy $Cu_2HgSn(Se_xS_{1-x})_4$ is less explored in this context. However, its Zn counterpart $Cu_2ZnSn(Se_xS_{1-x})_4$ has been investigated in detail (S. Chen et al., 2011).

In this work, we present the physical properties of $Cu_2HgSn(Se_xS_{1-x})_4$ alloy in detail on varying S and Se compositions at anion sites with random occupation for understanding the fundamentals of the emerging changes in different properties. We followed the first-principles approach to optimize the minimum energy-based lattice constants and to determine electronic and optical properties. A decreasing trend in electron effective mass and dielectric constant is noticed with increasing S content, and an excellent optical absorption strength of ~10^4 cm^{-1} is observed for most of the alloy compound semiconductors. We also noticed that the $Cu_2HgSn(Se_xS_{1-x})_4$ alloy material is more ductile than the $Cu_2ZnSn(Se_xS_{1-x})_4$ alloy (Z. Zhao & Zhao, 2015). Therefore, we must comprehend how specific characteristics, such as bandgap, effective masses, and dielectric constant, might vary. Except for the parent members, x = 0 and 1, we have not yet found a paper in the literature that discusses the optoelectronic properties of $Cu_2HgSn(Se_xS_{1-x})_4$ for the full x ($0 \le x \le 1$) range.

4.1 Computational Details

The full potential and linearly augmented plane wave (FPLAPW)(Wimmer et al., 1981) based WIEN2k code (Blaha et al., 2020) is used to perform density functional theory-based calculations to compute total energy, band structure, and optoelectronic parameters. We adopted the experimentally reported parameters for the parent compound $Cu_2HgSnSe_4$ in the literature for computing the electronic bandgap characteristics (Kabalov et al., 1998). We started with stannite $I\bar{4}2m$ space group structure and varied the composition ratio considering $1 \times 1 \times 1$ supercell with primitive structure and substituting S with Se via a random filling anion site. The compounds with S/Se concentrations are relaxed completely for 1mRy/Bohr force minimization utilizing GGA (Perdew et al., 1996) with PBEsol exchange-correlation functional. The plane wave cut-off-R^*K_{max}, charge density cut-off G_{max}, and the core valence separation are set as 8, 14 $(a.u.)^{-1}$, and -6 Ry, respectively, throughout the calculation. We sampled the 1000 k-points in the reduced Brillouin zone for self-consistent field calculations by fixing 0.001Ry/Bohr and 0.0001Ry force and energy tolerance. For computing accurate band structure and optical properties, we employed the modified Becke-Johnson (TB-mBJ) (Tran & Blaha, 2009) potential along with spin-orbit coupling. On viewing the strong onsite Coulomb interaction of Cu-3d and Hg-4d electrons, we considered the Hubbard parameter U= 0.52 Ry for all compositions found for the parent system in the literature (Vu et al., 2019). The elastic coefficients are computed with GGA using projector-augmented plane wave-based code VASP (Kresse & Furthmüller, 1996).

4.1 Result and Discussion

4.3.1 Structural Properties

The quaternary $Cu_2HgSn(Se_xS_{1-x})_4$ materials exhibit stannite tetragonal structure with space group $I\bar{4}2m$ crystallographic phase (Sarmadian et al., 2016). The structure exhibits an alternate stacking of Cu-Cu atoms after Hg-Sn atoms. An optimized crystal structure belonging to $Cu_2HgSnSe_{0.25}S_{0.75}$ is shown in Figure 4.1(a), and the others can be understood as the same crystal structure with different S/Se compositions. The tetragonal stannite phase of $Cu_2HgSn(Se_xS_{1-x})_4$ consists of two distinct Wyckoff positions for Cu atoms at 2c (0,0.5,0.25) and 2d (0.5,0,0.25) with Hg, Sn, and S/Se at 2a (0,0,0), 2b (0.5,0.5,0), and 8g (x, y, z), respectively. This structure remains analogous to the known stannite phase Cu_2ZnSnS_4 with slightly larger lattice parameters because of heavy cation Hg^{2+} in place of Zn^{2+} in the lattice.

Table 4.1: Comparison of calculated and experimentally reported lattice parameters for $Cu_2HgSn\ (Se_xS_{1-x})_4$ alloy.

Compositions	Our Calculation		Exp. Reported (Sarmadian et al., 2016)	
	a (Å)	c (Å)	a (Å)	c (Å)
Cu_2HgSnS_4	5.575	10.882	5.5749	10.882
$Cu_2HgSn\ (Se_{0.25}S_{0.75})_4$	5.621	11.011	-	-
$Cu_2HgSn\ (Se_{0.50}S_{0.50})_4$	5.690	11.153	-	-
$Cu_2HgSn\ (Se_{0.75}S_{0.25})_4$	5.760	11.274	-	-
$Cu_2HgSnSe_4$	5.823	11.389	5.822	11.822

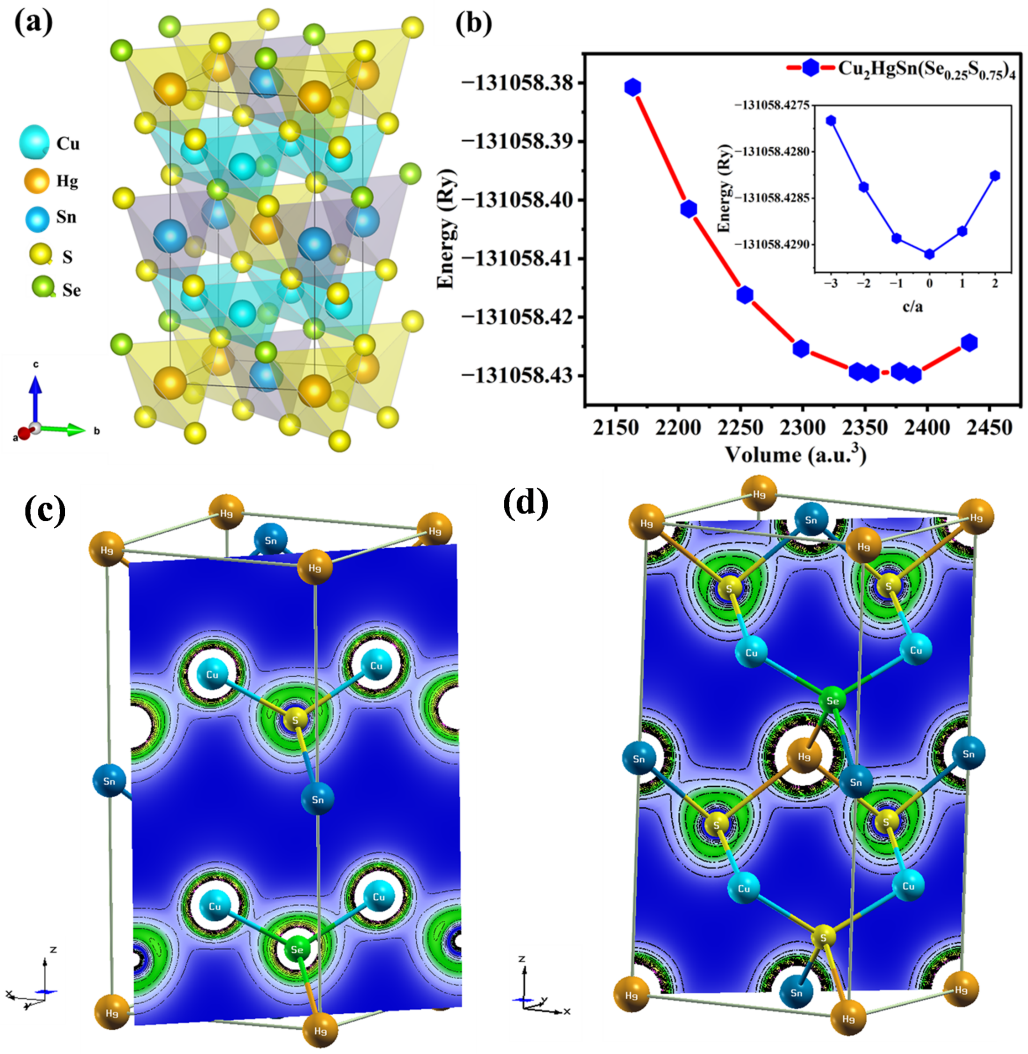


Figure 4.1 (a) Crystal structure of $Cu_2HgSn(Se_{0.25}S_{0.75})_4$ with polyhedral located off the ions (b) The volume energy curve for x = 0.25 with c/a vs. energy variation in the inset (c-d) The computed charge density along (0 1 1) directions signify the bonding character. More overlapping of electron density contour signifies a more covalent character.

The lattice parameters of optimized alloy structures of $Cu_2HgSn(Se_xS_{1-x})_4$ are summarized in Table 4.1, along with some reported experimental and theoretical data for comparison. A good match is observed for x = 0 and 1 compositions. The Murnaghan equation (Murnaghan, 1944) is used to fit the volume energy curve to extract the minimum energy, volume, and lattice parameters, as shown in Figure 4.1(b). The structure exhibits an alternate stacking of Cu-Cu atoms after Hg-Sn atoms with intertwined HgS_3Se-CuS_3Se-SnS_3Se tetrahedrons. We also carried out the Bader analysis (Henkelman et al., 2006; Yu & Trinkle, 2011) to determine different bond formations present in these tetrahedrons, as shown in Table 4.2. It signifies that all the ions (Cu^{+}, Hg^{2+}, Sn^{4+}, and S^{2-}) exhibit a robust covalent character within these geometries.

Additionally, S and Se atoms have an average excess charge of -0.76 e and -0.54 e, respectively, in $Cu_2HgSn(Se_xS_{1-x})_4$, indicating that unlike the S^{2-} ion, the Se^{2-} ion accepts less charge (-0.54 e) due to its comparatively less electronegative nature (L. C. Allen, 1989). Therefore, the bond length decreases in the presence of S ion, and lattice length increases with increasing Se concentration. Further on computing the charge density contour, the same observation is substantiated as found to be more overlapping, referring to the extensive sharing of electrons in

Cu-Se bond compared to Cu-S bond. Thus, the decrease in ionic character is noticed with increasing Se atomic fraction, i.e., x from 0 to 1.

Table 4.2: The Bader charge analysis for $Cu_2HgSn(Se_xS_{1-x})_4$ at x=0 and x=1. The charge at any atom is in the unit of elementary charge e and given by q_i; where i represents the atom.

Compositions	q_{Cu}	q_{Hg}	q_{Sn}	q_S or q_{Se}
Cu_2HgSnS_4	+0.55	+0.54	+1.48	-0.76
$Cu_2HgSnSe_4$	+0.38	+0.32	+1.10	-0.54

4.3.2 Elastic Properties

We also evaluated the elastic stiffness tensor (C_{ij}) to investigate the strength and stability of the material and to probe the mechanical stability together with the systems' bonding nature and flexibility for different Se concentrations (i.e., x values). The non-zero seven elastic coefficients must satisfy the Born-Huang criteria for the tetragonal system (Mouhat & Coudert, 2014) to confirm the mechanical stability of the $Cu_2HgSn(Se_xS_{1-x})_4$ compounds. We also computed various mechanical parameters such as Bulk modulus (B), which represents the volume compressibility; Young's modulus (Y), expressing the stiffness; Poisson's ratio (ν), describing the measure of plasticity, and the shear modulus (G), which measures the deformation of the system under transverse internal forces using the computed Cij coefficients. These mechanical parameters show a decreasing trend with increasing Se atomic fraction. It is attributed to the weaker Se bond compared to S bond, as the lattice parameters are also expanded accordingly.

Table 4.3: Compositional dependence of Young's modulus, Bulk modulus, and shear modulus (E, B, and G in GPa), Poisson's, Pugh ratio and Cauchy Pressure (ν,B/G, and C'), transverse ($\boldsymbol{\nu_t}$), longitudinal ($\boldsymbol{\nu_l}$), average ($\boldsymbol{\nu_m}$) velocities and Debye temperature (in K) elastic properties of $Cu_2HgSn(Se_xS_{1-x})_4$ at (x =0 to x=1.00).

	Composition (x)				
Parameter's	0.00	0.25	0.50	0.75	1.00
Young's modulus (E)	61.88	53.24	51.92	51.12	52.27
Bulk modulus (B)	74.32	72.67	68.38	66.17	66.65
Shear modulus (G)	22.73	19.32	18.90	18.64	19.08
Poisson's ratio (ν)	0.36	0.37	0.37	0.37	0.36
Pugh ratio (B/G)	3.27	3.76	3.61	3.54	3.49
Cauchy pressure (C')	35.6	40.4	36.8	33.8	32.5
ν_m (m/s)	2260.10	2036.57	1978.01	1931.81	1923.45
ν_l (m/s)	4306.22	4072.90	3902.08	3785.83	3748.35
ν_t (m/s)	2007.16	1804.53	1753.70	1713.27	1706.30
Debye Temperature (θ_D)	243.4	217.2	208.4	201.1	198.2

The values of mechanical parameters such as E, B, and G show a systematic decrease with Se concentration, as shown in Table 4.3. The change in B is relatively less compared to the E and G modulus. If the B/G ratio value is >1.75, the material is predicted to be ductile; otherwise, the material becomes brittle(Taylor & Pugh, 1954). We also computed the ν, and B/G ratio; both are increasing with Se concentration, revealing the increase in the ductile nature of the Se-rich compound. This increase is associated with reducing covalent bond strength with Se enrichment. Interestingly, The computed range of B/G value 3.27-3.76 is larger than the well-known Cu_2ZnSnS_4 (2.49), indicating that the $Cu_2HgSn(S/Se)_4$ film can be more flexible than the proposed Cu_2ZnSnS_4 (Deng et al., 2021) and can be used to materialize flexible solar cells.

Moreover, the positive and negative values of the Cauchy pressure (C') represent the ductile and brittle nature, and Se-rich compositions exhibit enhanced ductile nature. The Debye temperature is a crucial parameter of the solids at which all phonons are excited, and numerous physical properties, such as thermal conductivity, melting temperature, specific heat, etc., are associated with it. Anderson (Anderson, 1963) demonstrated that the Debye temperature could be calculated by the average velocity of sounds as follows:

$$\theta_D = \frac{h}{k_B}\left(\frac{3n}{4\pi}\frac{N_A\,\rho}{M}\right)^{\frac{1}{3}} \nu_m \tag{4.1}$$

Where,

$$\nu_m = \left[\frac{1}{3}\left(\frac{2}{\nu_t^3}+\frac{1}{\nu_l^3}\right)\right]^{-\frac{1}{3}}; \quad \nu_t = \sqrt{\frac{G}{\rho}} \;\; ; \;\; \nu_l = \sqrt{\frac{(3B+4G)}{3\rho}} \tag{4.2}$$

Where, h, k_B, N_A , n, and M are Planck's constant, Boltzmann's constant, and Avogadro's number, number of atoms per molecule, and molecular mass, respectively. The ν_t, and ν_l are the transverse and longitudinal sound velocities, respectively. The calculated values of ν_t, ν_l, ν_m, and θ_D are listed in Table 4.3 for $Cu_2HgSn(Se_xS_{1-x})_4$ systems. It is noted that θ_D appreciably decreases for substitutional alloying because the average sound velocity decreases. The detailed discussion of mechanical properties is reported by Kukreti et al (Kukreti, Ramawat, et al., 2023).

4.3.3 Electronic Properties

The evolution of the bands with different compositions is scanned to understand the change in the electronic properties of these compounds. There is no significant change in the band character, i.e., the direct bandgap is preserved for all values of x. Further, on considering the underestimation of bandgap values with GGA, the bandgap values are computed using mBJ + SO + U method for U= 7eV, which is considered in our previous work on Cu_2HgSnS_4, leading to the right bandgap value (Kukreti et al., 2021a). The computed band structure and the partial density of states are depicted in Figure 4.2 for all systems. An electronic bandgap appears along Γ-Γ high symmetry point in reciprocal lattice. The partial density of states suggest that the valence band edge comprises strongly hybridized Cu-d and S/Se-p orbitals, while the S/Se-p states populate most of the conduction band edge. Additionally, the contribution of other elements like Hg and Sn orbitals lies deep inside the bands. This is also consistent with the parent $Cu_2HgSn(S/Se)_4$ semiconductors and illustrated in other study (Vu et al., 2020).

Interestingly, instead of Hg-s and S/Se-p state hybridization, the Se states dominate most of the conduction band edge side. Its impact increases with increasing Se concentration. As a result, the conduction band edge is lowered, simultaneously changing its curvature effectively from x=0 to x=1. In contrast, Cu-d orbitals dominate for any x composition in the edge of the valence band. However, a slightly increased Se contribution is also visible in this valence band edge, causing a slight downshift in the valence band, with the curvature exhibiting a slight decrease throughout the variation.

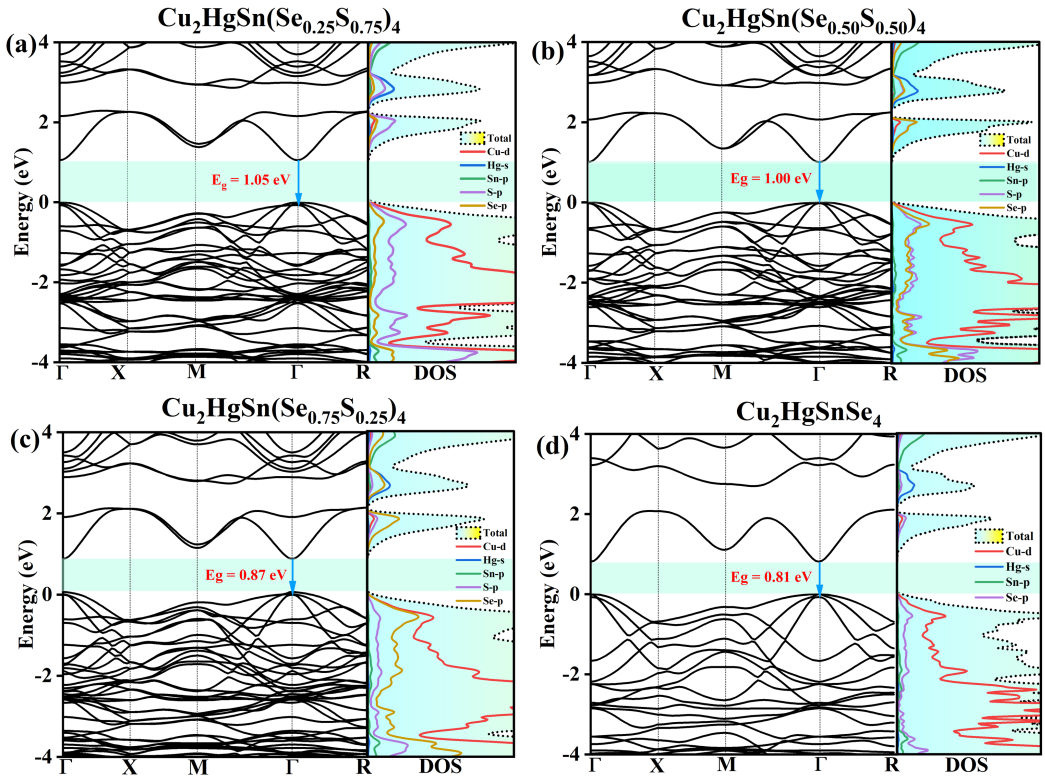


Figure 4.2 (a-d) Electronic band structure of $Cu_2HgSn\ (Se_xS_{1-x})_4$ at x =0 to x=1.00 with partial density of states of different orbitals of ions. The increase in Se concentration appears to dominate on the conduction band side. A partial contribution Se also emerges on the valence band edge but with the most dominated Cu-d states.

4.3.4 Lattice Parameter and Band Gap Bowing

The bandgap changes monotonically with composition in alloy systems but not linearly over the whole range (Barone et al., 2022; S. Chen et al., 2011). For $Cu_2HgSn(Se_xS_{1-x})_4$ systems, as heavy element Se concentration increases, bandgap decreases monotonically from 1.33eV at x = 0 to 0.811 eV at x = 1 with a small bowing in bandgap with composition, Figure 4.4 (a). The computed bandgap variation is fitted using the Vegard's law (Kuo et al., 2004);

$$E_x = xE_g(CHTSe) + (1-x)E_g(CHTS) - bx(1-x) \tag{4.3}$$

Where E_g is bandgap, and b is the bowing parameter for the bandgap. The small bowing, i.e., b = 0.395 eV is noticed for $Cu_2HgSn(Se_xS_{1-x})_4$ mixed-anion alloy (see Figure 4.3a) and is attributed to the slight difference in the size of S and Se atoms. Further, the lattice parameter is also fitted with Vegards' law as

$$a(x) = xa(CHTSe) + (1-x)a(CHTS) - bx(1-x) \tag{4.4}$$

and very small bowings of ~ 0.387 and 0.055 Å are noticed for a and c lattice parameters, respectively, Figure 4.3 (b & c).

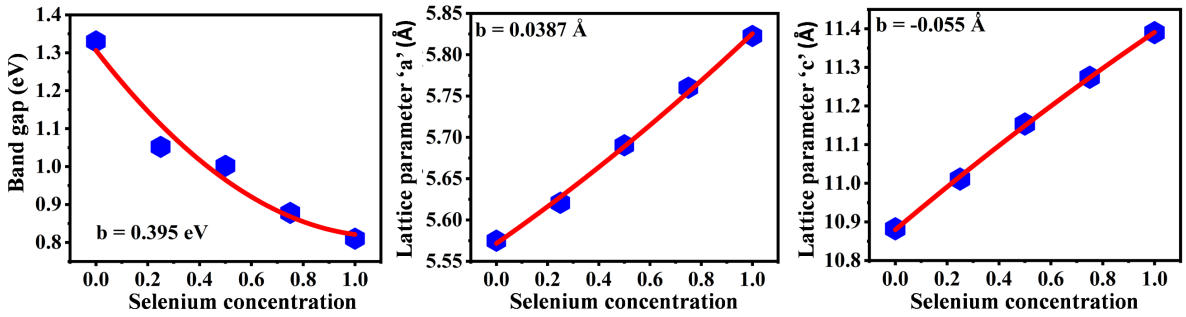


Figure 4.3 (a) The variation of Se composition on bandgap and lattice parameters are fitted. Bandgap bowing, (b, c), lattice parameter 'a' bowing, and lattice constant 'c' bowing.

4.3.5 Optical Properties

The optical parameters, i.e., dielectric function $\varepsilon(\omega)$ absorption $\alpha(\omega)$, and refractive index $n(\omega)$, are studied over perpendicular and parallel directions to the c-axis and tabulated in Table 4.4. These optical constants are relevant when analyzing their applicability as a photo-absorber material for solar photovoltaics and photodetector devices. The computed real $\varepsilon^1(\omega)$and imaginary part $\varepsilon^2(\omega)$ of the complex dielectric function $\varepsilon(\omega) = \varepsilon^1(\omega) + i\varepsilon^2(\omega)$ are presented in Figure 4.4. The imaginary part of the dielectric function gives the idea about the absorption inside the material; however, the real part introduces the degree of polarization under an electric field. Besides, the real part of the dielectric constant at zero frequency is used to define the static dielectric constant, $\varepsilon^1(0)$. Considering the uniaxial anisotropy, perpendicular and parallel components, i.e., $\varepsilon^1_{xx}(\omega)$, $n^1_{xx}(\omega)$, $\alpha^1_{xx}(\omega)$, and $\varepsilon^1_{zz}(\omega)$, $n^1_{zz}(\omega)$, $\alpha^1_{zz}(\omega)$, are evaluated, and perpendicular components are depicted in Figure 4.4. The order of absorption coefficient magnitude remains ~10^4 cm^{-1} for all values of x, while the absorption edge exhibits red-shifted with increasing x. It is consistent with the noticed electronic bandgap variations against x. The absorption edge lies in the 1.33 to 0.8 eV range and could be a suitable alloy absorber for AM-1.5 spectrum when used as a graded absorber in a solar cell.

We also observed a higher polarization strength by noticing the increase in static dielectric constant values with more selenium concentration, which is a good sign for electron-hole pair dissociation from the photoinduced excitons for their use in solar cells. The plasmon oscillations are also noticed at crossing zero value by $\varepsilon^1(\omega)$ curve and shown in Table 4.4. It indicates the plasma oscillation or metallic nature after a particular frequency. The dispersion in the refractive index with varying x is visible in Figure 4.4 (d), and the increasing trend is evident because of the increased dielectric function.

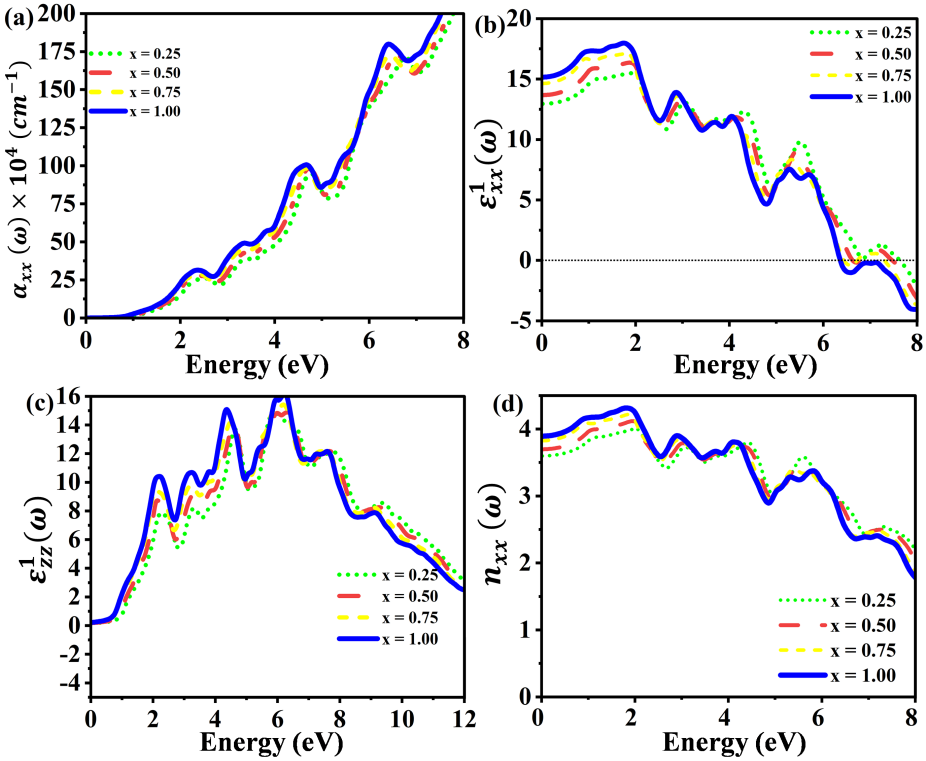


Figure 4.4 (a-d) The absorption coefficient of $Cu_2HgSn(Se_xS_{1-x})_4$ at x=0.25 to x=1 with real (ε^1_{xx}) and imaginary part (ε^2_{xx}) of the dielectric function, the refractive index function in the perpendicular direction to the c-axis. A significant increase in the degree of polarization and the refractive index is noticeable along the x direction when Se enriches.

Table 4.4 The computed optical constants for $Cu_2HgSn(Se_xS_{1-x})_4$ at x=0.25 to x=1.

Compositions (x)	E_g(eV)	$\varepsilon^1_{xx}(0)$	$\varepsilon^1_{zz}(0)$	$\varepsilon^1_{ave}(0)$	ω^p_{xx}	ω^p_{zz}	$n_{xx}(0)$	$n_{zz}(0)$
$Cu_2HgSn(Se_{0.25}S_{0.75})_4$	1.052	12.95	14.81	13.88	7.60	7.60	3.60	3.85
$Cu_2HgSn(Se_{0.50}S_{0.50})_4$	1.000	13.67	15.61	14.64	6.59	7.36	3.67	3.95
$Cu_2HgSn(Se_{0.75}S_{0.25})_4$	0.878	14.63	16.58	15.60	6.43	7.22	3.82	4.07
$Cu_2HgSnSe_4$	0.811	15.15	16.94	16.04	6.35	6.27	3.93	4.12

4.3.6 Impact of Bowing on effective mass and dielectric constant

We observed a decreasing trend in electron effective mass with increasing x, i.e., Se concentration, while a slight variation (almost constant) for hole effective mass with x is noticed. The nearly constant hole-effective mass is attributed to the less affected curvature on the valence band edge in the electronic band structure. In contrast, the increased curvature of the conduction band edge due to the introduction of Se-p states is the main source of lowering the electron effective mass with increasing Se concentration. On the other side, average dielectric constant values enhance with increasing Se composition. This is consistent with the literature and attributed to the increased unit cell size. Therefore, selenium-rich alloys are more prone to polarization.

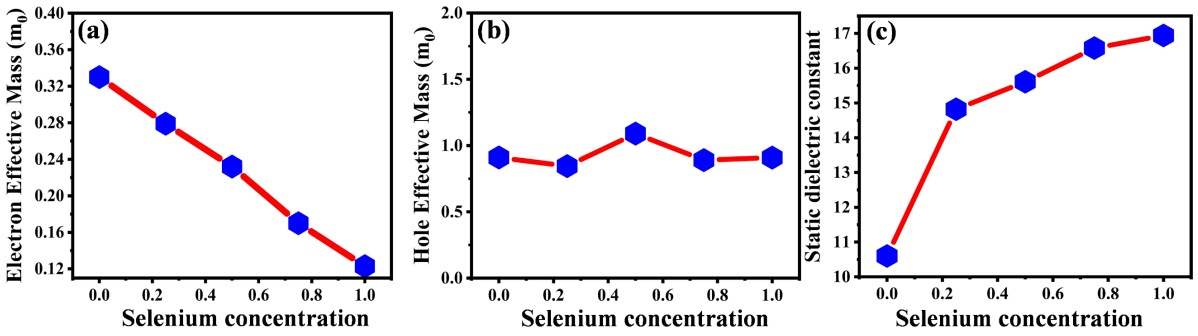
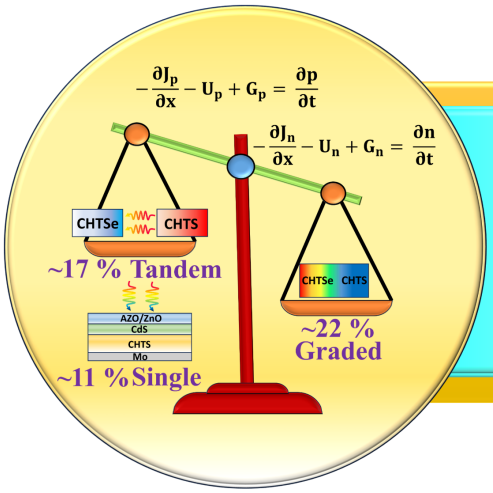


Figure 4.5 Compositional dependence of the effective mass of (a) electron m_e, (b) hole m_h, and (c) variation in static dielectric constant.

4.4 Conclusion

On investigating the bandgap engineering with Se alloying in Cu_2HgSnS_4, i.e., $Cu_2HgSn(Se_xS_{1-x})_4$ compounds, a bandgap variation in the range of 1.33 to 0.81 eV is demonstrated from x = 0.00 to 1.00 compositions. The elastic constant satisfies the Born-Haung criteria, revealing the ductile nature of $Cu_2HgSn(Se_xS_{1-x})_4$, thus making it a good candidate for flexible optoelectronic devices. The small size difference in S and Se atoms gives rise to the slight bowing in bandgap and a significant reduction in electron effective mass 'm_e' because of the increased curvature. In contrast, hole effective mass 'm_h' is nearly insensitive to the Se concentration. The absorption coefficient is of the same order (~ 10^4 cm^{-1}) for all compositions, with a red-shifted absorption edge for the selenium-rich compounds. The bandgap in visible to infrared regions with suitable optoelectronic properties makes $Cu_2HgSn(Se_xS_{1-x})_4$ alloy systems ideal for solar cell and multispectral photodetector applications. The low bandgap alloy systems may also be potential candidates for thermoelectric devices. Further, the large variation in bandgap can also be harnessed for the graded and tandem junction photovoltaics. Thus, the present study may provide a novel semiconducting material platform for numerous optoelectronic and thermoelectric devices.



Drift-Diffusion modelling of solar cell

- ✓ Single Junction
- ✓ Tandem junction
- ✓ Graded Bandgap absorber